University of Plymouth

PEARL **https://pearl.plymouth.ac.uk**

01 University of Plymouth Research Outputs University of Plymouth Research Outputs

2016-12-01

Physical modelling of wave scattering around fixed FPSO-shaped bodies

Mai, T

http://hdl.handle.net/10026.1/8508

10.1016/j.apor.2016.10.007
Applied Ocean Research

All content in PEARL is protected by copyright law. Author manuscripts are made available in accordance with publisher policies. Please cite only the published version using the details provided on the item record or document. In the absence of an open licence (e.g. Creative Commons), permissions for further reuse of content should be sought from the publisher or author.

"This is the author's accepted manuscript. The final published version of this work (the version of record) is published by Elsevier in Applied Ocean Research available at: 10.1016/j.apor.2016.10.007. This work is made available online in accordance with the publisher's policies. Please refer to any applicable terms of use of the publisher."

Physical Modelling of Wave Scattering Around Fixed FPSO-Shaped Bodies

T. Mai[1,*], D. Greaves[1], A. Raby[1], P. H. Taylor[2]

[1] *School of Marine Science and Engineering, Plymouth University, Plymouth, Devon, United Kingdom, PL4 8AA*

[2] *Department of Engineering Science, University of Oxford, Oxford, United Kingdom, OX1 3PJ*

ABSTRACT

FPSO (Floating Production Storage and Off-loading) vessels used for offshore oil and gas production are operated in deep water, often at locations which experience severe wave loading. This paper reports on laboratory experiments on a series of simplified FPSO-shaped bodies, with the aim of understanding more about the wave-structure interaction, particularly the generation of scattered waves. These tests were carried out in the Ocean Basin at Plymouth University's COAST Laboratory where the effects on the wave-structure interaction of model length, wave steepness and incident wave direction were investigated. All three models had semi-circular ends, separated by a box section for the 2 longer models. Input waves were based on focused wave groups generated using NewWave with an underlying JONSWAP spectrum. A general phase-based harmonic separation method was applied to separate the linear and higher-harmonic wave components of the free-surface elevation surrounding the bodies, and of relevance to the assessment of wave loads. Close to the bow of the model, the highest amplitude scattered waves are observed with the most compact model, and the third- and fourth-harmonics are significantly larger than the equivalent incident bound harmonic components. At the locations close to the stern, the linear harmonic is found to increase as the model length is decreased, although the nonlinear harmonics are similar for all three tested lengths, and the second- and third-harmonics are strongest with the medium length model. The nonlinear scattered waves increase with increasing wave steepness and a second pulse is evident in the higher-order scattered wave fields. As the incident wave angle between the waves and the long axis of the vessel is increased from 0 (head-on) to 20 degrees, the third- and fourth-harmonic scattered waves reduce on the upstream side. These third- and fourth-harmonic diffracted waves should be considered in assessing wave run-up for offshore structure design, and may be relevant to the excitation of ringing-type structural responses in fixed and taut moored structures.

Keywords: physical model, nonlinear, diffraction, FPSO, ringing

1 Introduction

Wave-induced load components at integer harmonics of the dominant linear input wave frequency can excite high frequency resonant responses for floating offshore structures (e.g. floating offshore

[*] Corresponding author.

E-mail address: tri.mai@plymouth.ac.uk (Tri Mai)

wind turbine, floating wave energy converter, floating production storage and off-loading vessels - FPSOs and floating platforms more generally) and also for bottom-fixed offshore structures (e.g. gravity-based structures - GBS). There may be a nonlinear transfer of energy to a higher-harmonic response of the structure owing to nonlinear wave-wave interaction effects and nonlinear wave-structure interaction effects. Therefore, waves with the incident spectral energy at peak frequency (f_p) can in principle excite structural responses at multiples of the linear peak frequency ($2f_p$, $3f_p$, $4f_p$ ...). These higher-harmonic frequencies are known to cause highly intense nonlinear structural behaviours called *springing* (at double frequency) and *ringing* (at triple), which were first observed in a model test of the Hutton platform which was operated in the UK North Sea from 1984-2001 (Mercier, 1982). The second-order excitation at the double frequency dominates for springing, while the higher-order (3rd and 4th order) frequencies trigger the ringing of gravity-based platforms and tension leg platforms, which is a transient elastic response (Faltinsen, 1995 & 2014). Shao and Faltinsen (2014) used a new potential flow method (the harmonic polynomial cell method) to simulate the linear and higher-order harmonic force amplitudes and phases on a surface-piercing vertical cylinder standing on the sea floor in regular waves. Their results showed good agreement with the higher-harmonic experimental results by Huseby and Grue (2000). Bachynski and Moan (2014) simulated wave-structure interaction of different tension leg platform used to support wind turbines and their simulation results showed that the large extreme forces were caused by ringing loads, which also increased short-term fatigue damage in the tendons and tower.

Floating Production Storage and Off-loading (FPSO) vessels are important and commonly used as parts of offshore oil and gas production systems. In recent decades, oil and gas resources are being developed in increasingly deep water and it is necessary to understand wave-FPSO interactions in such water conditions, and physical model testing remains important. The interaction of waves with an FPSO-type body has been the subject of previous investigations, for example the wave scattering (Zang et al., 2006; Siddorn, 2012) and the response of an FPSO vessel in long- and short-crested seas (HR Wallingford Ltd, 2002). Zang et al. (2006) examined the effects of second order wave diffraction around the bow of a simplified FPSO. Their study found at locations upstream of the bow there is a second order bound harmonic of the incoming wave, then later radiated free waves well-separated from the incoming wave group, but no significant third-order harmonic components were observed. A significant second-order diffracted wave field was found in the fully nonlinear simulations of Siddorn (2012) based on a boundary element potential flow method with quadratic elements, but again no evidence of the third-harmonic contributions at the bow or upstream. However, there was evidence of third-order diffraction off out to the sides and diagonally downstream of the stern of the FPSO.

Fitzgerald et al. (2014) studied higher harmonic diffracted wave fields around a surface-piercing column due to a focused wave group using NewWave theory (Tromans et al., 1991). They simulated wave-structure interaction of a focused wave group (with kA = 0.1, where k is the wavenumber corresponding to the spectral peak energy period, and A is the total amplitude of the linear harmonic) and a 0.25 m diameter cylinder, using a fully nonlinear higher-order BEM potential flow model. Their simulation showed the second and third harmonics of the total and scattered wave fields at locations upstream and downstream of model. Their general phase-based harmonic separation method (Fitzgerald et al., 2014) will be applied to decompose the local wave field in this paper.

Experiments were carried out using three FPSO models of different lengths; with waves of various steepness and with incident waves approaching from three different angles. The scattered wave field around the fixed models is investigated in detail by applying the phase-based harmonic separation method to separate the harmonic components of the scattered wave. The linear, second, third and fourth harmonics of the evolution of the local wave field and the scattered wave amplitudes are presented and discussed.

2 Methodology

2.1 Experiment

The experimental work was carried out in the Ocean Basin at Plymouth University's COAST Lab. The ocean basin is 35 m long by 15.5 m wide and has a movable floor that allows operation at different water depths. A water depth of 2.93 m was used for this experiment. The FPSO models were made of aluminium and were fabricated at ~1:100 scale from a rectangular box with a half circular cylinder at the bow and stern for the longer models (Model 2 and 3) and purely a cylinder for Model 1. The tested models all had the same height and width of 0.3 m, and lengths of 0.3 m, 0.6 m and 1.2 m (Figure 1). The draft was 0.15 m for all of the models. The models were rigidly fixed to the gantry, which spans the width of the Ocean Basin.

The input waves were focused wave groups generated using the NewWave methodology (Tromans et al., 1991) with an underlying JONSWAP spectrum ($\gamma = 3.3$), focusing at the bow of the models. Hence, the input wave group is a representation of the average shape of the largest (linear) waves in a random sea-state with a JONSWAP spectrum. A set of non-breaking wave conditions, which correspond to the 100-year extreme significant wave height at the Cleeton platform in the Southern North Sea (Williams, 2008), were employed in these experiments by scaling (1:100). The peak wave periods were chosen according to the guidance of the offshore technology report for UK water (Offshore Technology Report, 2001) to have a variety of wave steepness for investigation. The local wave steepness varied from 0.13 to 0.21, and the incident wave angle was from 0° to 20° where 0° corresponds to a head sea. The ratio of wavelength (corresponding to T_p) over body size varies between ~2.3 (longest model) and ~10 (cylinder). Test parameters are given in Table 1. Wave run-up on the models and the local wave field around the models were measured by 24 resistance wave gauges (Figure 2) with a sampling frequency of 128 Hz.

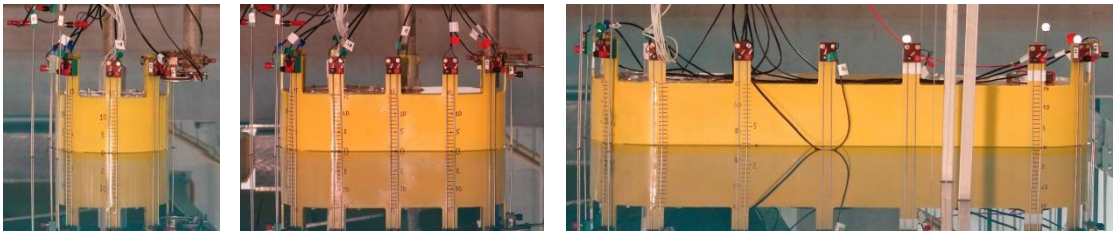

Model 1 Model 2 Model 3

Figure 1. The tested models in the Ocean Basin.

Table 1. The tested wave conditions.

Parameters	Values

Amplitude, A (m)	0.069 - 0.094
Peak period, T_p (s)	1.330 - 1.440
Peak energy frequency, f_p (Hz)	0.694 - 0.750
High frequency cut-off (Hz)	2
Wave steepness, kA (-)	0.13 - 0.21
Wave direction, α (°)	0 - 20
Water depth, d (m)	2.93
Relative depth, kd (-)	5.68 - 6.63

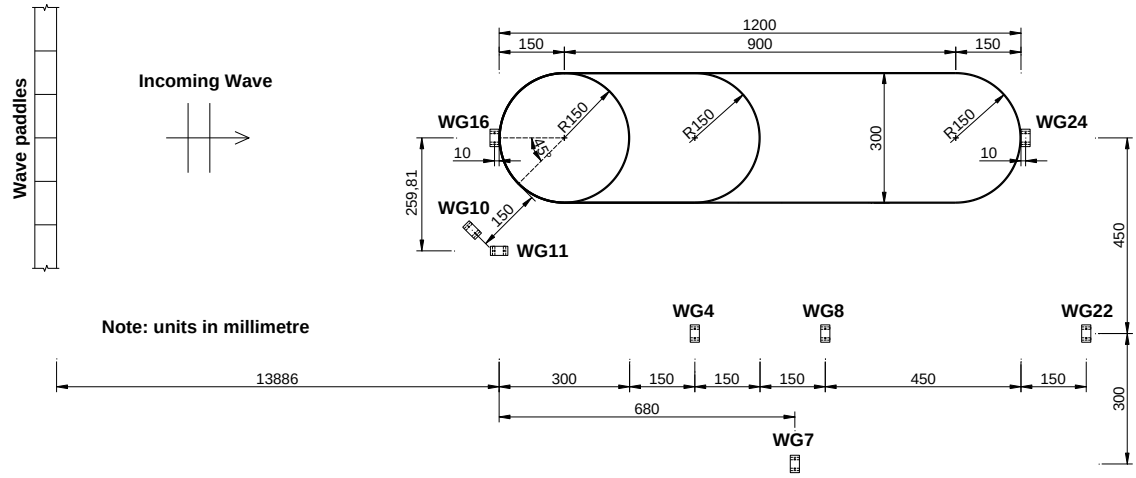

Figure 2. Layout of wave gauges around the tested models.

2.2 Phase-based harmonic separation method

The higher-harmonic components of the free-surface elevation could have been separated using the *phase-inversion* methodology first presented by Baldock et al. (1996). For applications see Hunt et al. (2003), Borthwick et al. (2006), Zang et al. (2006), Siddorn (2012), Fitzgerald et al. (2014) and Hann et al. (2014). The odd and even harmonic components can be extracted from the time histories of kinematic or dynamic quantities i.e. the free-surface elevation or wave force in the focus wave group interactions, in which two incident wave groups have identical wave component amplitudes and frequencies but inverted phase i.e. phase of 0° (crest-focused wave) and 180° (trough-focused wave). Then the individual harmonics e.g. linear and third-order, or second- and fourth-order can be separated from each other by frequency filtering.

In this paper, the extended phase-based harmonic separation method (Fitzgerald et al., 2014) is applied to extract the linear and higher-order harmonic components of the free-surface elevation by applying simple linear combinations of the relevant time histories. This method requires the data from four incident focused wave groups that are each exactly 90° out of phase. There is then minimal post-processing applied to extract the linear, second-, third- and fourth-harmonics.

An incident wave group that has amplitude A and relative phase θ can be expressed as the classic Stokes perturbation expansion (Fenton, 1985), as follows

$$\eta(A,\theta) = B_{11}A\cos\theta + A^2(B_{20} + B_{22}\cos 2\theta)$$
$$+A^3(B_{31}\cos\theta + B_{33}\cos 3\theta) + A^4(B_{40} + B_{42}\cos 2\theta + B_{44}\cos 4\theta) + O(A^5) \qquad (1)$$

where B_{ij} are the coefficients in Fourier series for $\eta(A,\theta)$; i is the amplitude content order; and j is the frequency content order. Equation (1) can be rewritten in a more compact form as:

$$\eta(A,\theta) = \eta_{11} + (\eta_{20} + \eta_{22}) + (\eta_{31} + \eta_{33}) + (\eta_{40} + \eta_{42} + \eta_{44}) + O(A^5) \qquad (2)$$

where, η_{ij} are the jth-order harmonic components, $\eta_{ij} = A^i B_{ij} \cos(j\theta)$. If i and j are identical, then η_{ij} are the jth-order harmonic sum, e.g. the first-order sum η_{11}. On the other hand, if i and j are different, then η_{ij} are the jth-order harmonic difference, e.g. the term η_{31} is at the first-harmonic in frequency but 3rd order (cubic) in input wave amplitude. Henceforth, we refer to the subscript i as the (amplitude) order and j as the harmonic.

By considering four focused wave groups generated from the same wave amplitude components but with the phase of each Fourier component shifted 0°, 90°, 180° and 270° it is possible to obtain the four time histories of free-surface elevation η^0, η^{90}, η^{180} and η^{270} respectively. The linear combinations of these time histories and the Hilbert transforms of the 90° and 270° free-surface elevation time histories are applied to extract the linear and the first three superharmonics (2nd, 3rd and 4th order); these are important for springing and ringing and are presented in Equations (3) - (6). A more detailed explanation of the separation method can be found in Fitzgerald et al. (2014).

$$(\eta^0 + H(\eta^{90}) - \eta^{180} - H(\eta^{270}))/4 = \eta_{11} + \eta_{31} \quad (3)$$

$$(\eta^0 - \eta^{90} + \eta^{180} - \eta^{270})/4 = \eta_{22} + \eta_{42} \quad (4)$$

$$(\eta^0 - H(\eta^{90}) - \eta^{180} + H(\eta^{270}))/4 = \eta_{33} \quad (5)$$

$$(\eta^0 + \eta^{90} + \eta^{180} + \eta^{270})/4 = \eta_{20} + \eta_{40} + \eta_{44} \quad (6)$$

where H is the harmonic conjugate of the signal. We note that due to the relatively weak nonlinearity of the difference components compared with the sum components, for example η_{31} compared with η_{11}, the difference components are likely to be negligible. The only exception to this is the 0th-order component η_{20} which represents the long wave set-*down* and can be cleanly separated using digital frequency filtering from components obtained in Equation (6). This long wave set-down also contains a 4th-order amplitude contribution η_{40} but in this application this additional contribution is small compared to the 2nd order term.

Figure 3 shows the time histories of the free-surface elevation η^0, η^{90}, η^{180} and η^{270} at the focus location (wave gauge WG11). The vertical axis is the dimensionless free-surface elevation (η/A), where η is the free-surface elevation and A is the linear amplitude at the focus location and time. The horizontal axis is the time scale with the focus time at $t = 0$ s. The focused wave groups shown in Figure 3 have a spectral peak energy period $T_p = 1.44$ s and total linear amplitude A of 0.069 m, the wave steepness is then $kA = 0.13$, where k is the wavenumber corresponding to T_p.

Applying the linear combinations presented in Equation (3) - (6) for η^0, η^{90}, η^{180} and η^{270} in Figure 3, the linear and the next three higher harmonic components have been obtained and presented in terms of their normalised amplitude spectra (Figure 4) and their separated time histories (Figure 5). It should be noted that we refer to plots such as Figure 4 as amplitude spectra, more precisely such plots show the modulus of the amplitude of each Fourier component as a function of frequency. Minimal post-processing (Fourier bandpassing) has been applied to remove the leakage of the linear component in the higher harmonics. The higher-order sum frequency components ($\eta_{22}+\eta_{42}$, η_{33}, η_{44}) are derived from the experiments by applying the fast Fourier transform (FFT) to the measured data, removing the zero-frequency and linear frequency range of the amplitude spectrum, leaving the higher-order sum frequency ranges individually, and then performing an inverse FFT. Consequently, the linear and higher-order sum harmonic components are very well separated using the extended phase-based harmonic separation method with a minimal post-processing. There was a

double frequency error wave train off the wave paddles since only linear wave theory was used to create the waves. This can be seen at around t = +13 s for the second harmonic presented in Figure 5b.

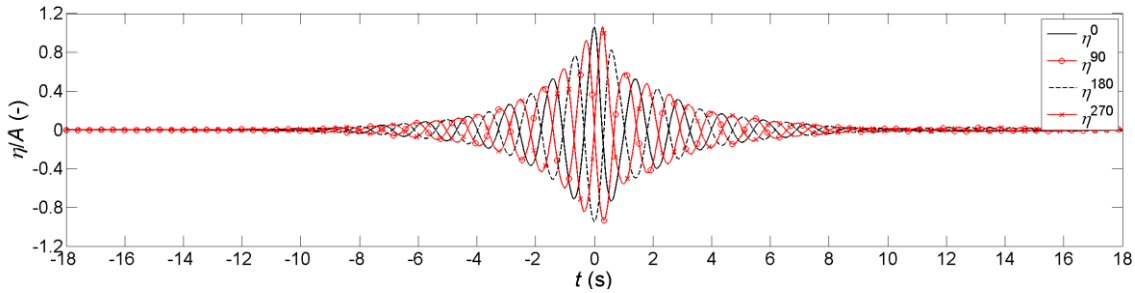

Figure 3. Wave profiles at the focus location (without model, kA = 0.13).

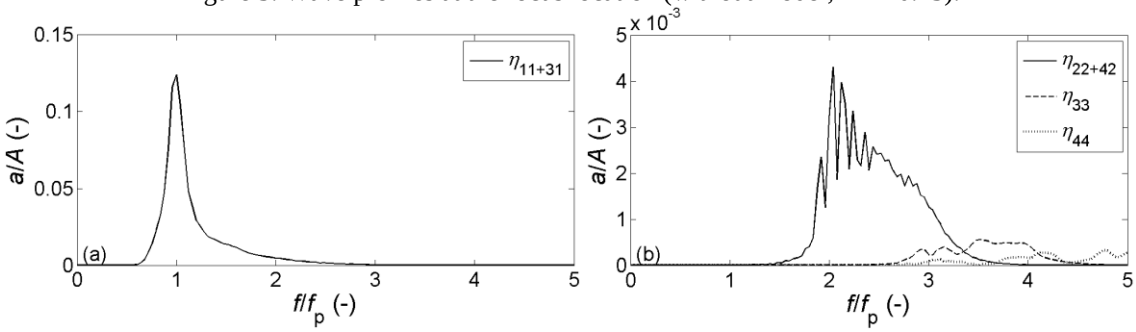

Figure 4. Amplitude spectra of the separated components at the focus location (without model, kA = 0.13). Note the different vertical scales.

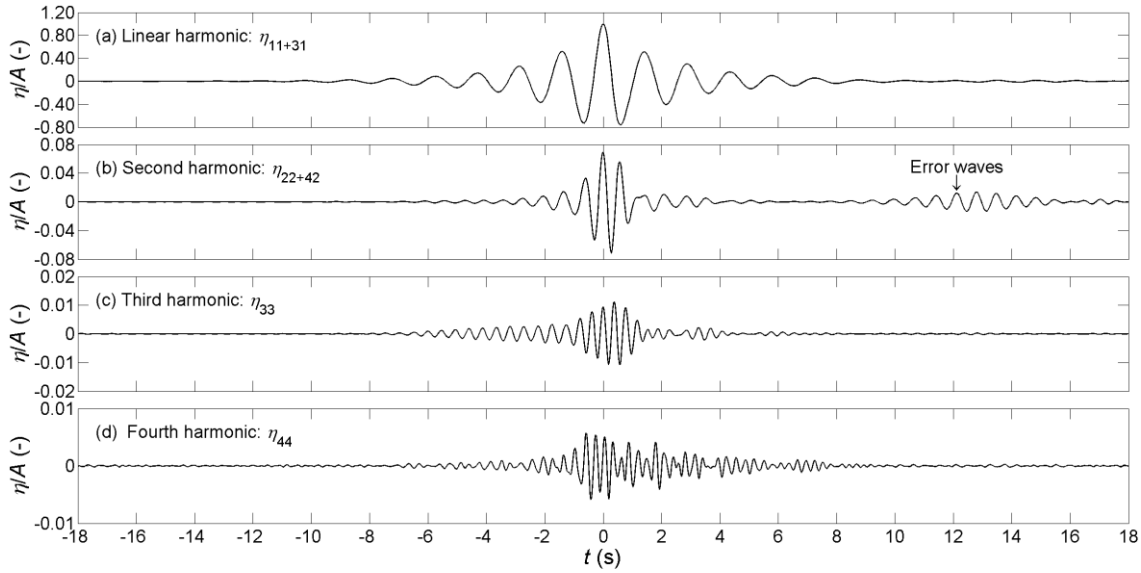

Figure 5. Time histories of the separated components at the focus location (without model, kA = 0.13). Note the different vertical scales.

2.3 Scattered wave field

The scattered or diffracted wave field can be simply extracted as the difference between the undisturbed incident wave and the measured wave in the presence of the model as follows

$$\eta_{ij}^{dif} = \eta_{ij}^{Model} - \eta_{ij} \,, \tag{7}$$

where η_{ij}^{dif} is the $(i,j)^{th}$ component of the scattered/diffracted wave, η_{ij}^{Model} is the equivalent component with the model present, and η_{ij} is the undisturbed incident wave component measured at the same gauge location in the absence of the model.

2.4 Uncertainty and repeatability

Resistance wave gauges were used in the experiments. When the gauge operates, the resistance of the water between a pair of parallel rods/wires is measured and this is proportional to the immersion depth. The gauges were calibrated at the beginning of each test day and/or before the tests with each model in place. The linearity of the gauge measurement is very close to 1 over the entire range of surface elevation measured in the experiments. Repeatability of the unprocessed time history of measured water elevation at the presented locations is very high and is repeatable within the thickness of a line.

In the experiments, the focus location was predefined at the bow stagnation point. With each focus wave group, the input focus distance for the (linear) wave paddle was optimised to ensure that the waves focus at the predefined location without the FPSO model in place. The focus location was determined to be the point at which the troughs either side of the central crest are symmetric, i.e. of equal depth. WG11 was used to measure water elevation at the focus location. The input focus distances of the wave groups with kA = 0.13, 0.18 and 0.21 were 13.56 m, 13.25 m and 15.365 m, respectively. From the measured signals at WG11, the focused time t_f of each wave group was determined and then the time shift Δt_f estimated. Each wave group has it group velocity c_g (a half of the phase velocity c_p), therefore the shift of the focus point is calculated by $\Delta X_f = c_g * \Delta t_f$. Consequently, the shift of the focus point is about 0.1 m between the wave groups with kA = 0.13 and 0.18 or about 2.5 m between the wave groups with kA = 0.18 and 0.21.

It should be noted that unless very steep near breaking waves are generated, the movement of the focus position and changes in wave structure are group properties - relative phase of the components is important but not absolute phase. Hence, the crest-trough phase combination will still work, and of course it would become immediately clear from the analysis if it was to breakdown - with large leakage of even harmonics into the odd harmonics. Although the harmonic extraction process is sensitive to the accuracy of the time alignment of the four phase combinations, the results presented here are very clearly separated between the different harmonics and there is no significant leakage between harmonics.

3 Results

3.1 Effect of model length on wave scattering

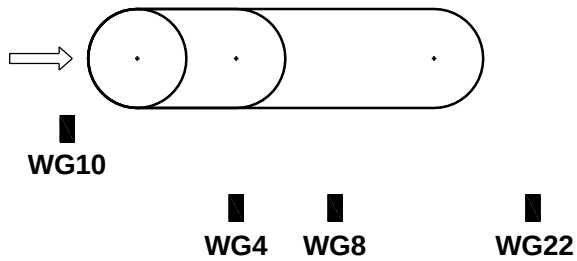

Figure 6. Location of WG4, 8, 10 & 22 for models 1, 2 & 3.

Wave gauges were positioned close to the tested models (see Figure 1) in order to examine how the model length affects the scattered wave field. Two locations were investigated, close to the bow (WG10) and at a fixed distance from the stern of the three models (WG4 for Model 1, WG8 for Model 2 and WG22 for Model 3), as shown in Figure 6, with exact gauge locations given in Figure 2. Results are presented for the steepest wave (kA = 0.21).

3.1.1 Near the bow

By applying the phase-based harmonic separation method introduced in Section 2.2, the linear and the higher harmonic components of the free-surface elevation ($\eta_{22}+\eta_{42}$, η_{33}, η_{44}) can be obtained at the bow of the models (for WG10 just upstream of the front stagnation point on the bow). The amplitude spectra that correspond to the time history of the separated components are shown in Figure 7. Comparing these spectra for the tests with and without the models in place indicates the considerable enhancement of the spectra due to the interaction of the incident waves with the models. This is evident in the importance of the second, third and fourth harmonics. In addition, it is found that the enhancement of the amplitude spectrum of the higher harmonics ($\eta_{22}+\eta_{42}$, η_{33}, η_{44}), due to wave interaction with Model 1 (the cylinder), are strongest in comparison with the interactions observed with Models 2 and 3. The amplitude spectra of the linear and higher harmonics caused by the presence of Models 2 and 3 are approximately the same, except the second harmonic (η_{22}), which is greater for Model 3 than for Model 2.

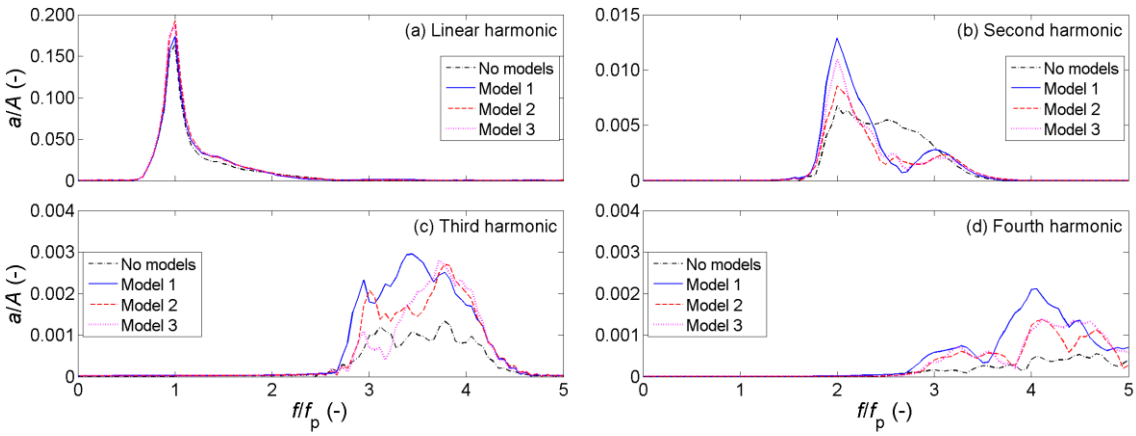

Figure 7. Amplitude spectra of the separated components near the bow of the models for kA = 0.21 (WG10). Note the different vertical scales.

The corresponding time histories of the separated harmonic components are derived by performing an inverse FFT of the corresponding filtered amplitude spectrum. These are presented in Figure 8 for the waves with and without the models in place. Significant enhancement of the free-surface elevation of the linear and higher harmonics due to wave scattering from the models can be clearly seen. The local free-surface elevation of the linear component has a lower crest and higher trough, in the presence of Model 1, than with Models 2 and 3 in place (Figure 8a). In contrast, the local free-surface elevations of the second, third and fourth harmonics have the highest crest and lowest trough with Model 1 and these are approximately the same with Models 2 and 3 (Figure 8b, c, d). For the second harmonic, the incident bound and scattered wave fields are roughly comparable (Figure 8b). However, the third and fourth harmonics indicate that the scattered wave field is significantly larger than the incident bound wave component (Figure 8c, d).

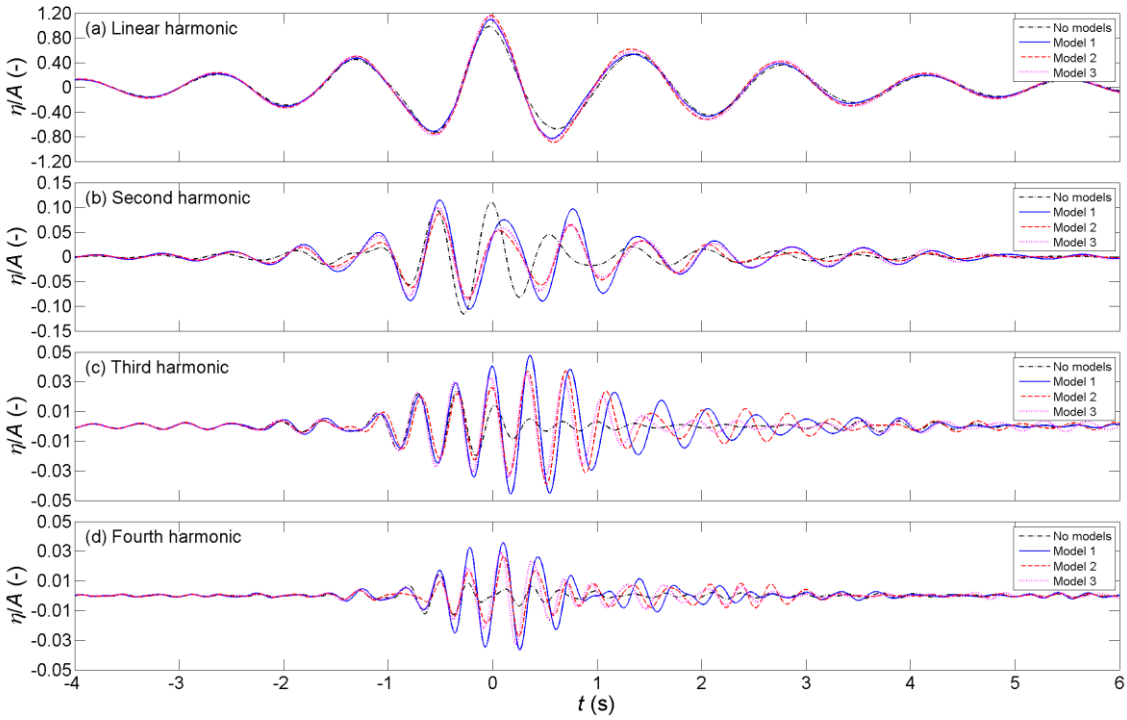

Figure 8. Time histories of the separated components near the bow of the models for kA = 0.21 (WG10). Note the different vertical scales.

Data on the scattered wave only are obtained by subtraction of the time histories with and without the models in place (Equation (7)); these are shown in Figure 9. As previously seen in Figure 8, the scattered waves of the second, third and fourth harmonics are strongest with Model 1 in place (Figure 9b, c, d). The third harmonic scattered wave is reduced as the model length is increased. It can be observed in Figure 9c & d that there is a second pulse in the third and fourth harmonics of the scattered wave fields, arriving about 1.5 s later than the first pulse. This may induce a second load cycle for the structure. It should be noted that this is entirely separated from the double frequency error wave off the paddles which arrived at the model at around t = +13 s in the time histories of the second harmonic components (Figure 5b), and will then diffract in a predominately linear manner.

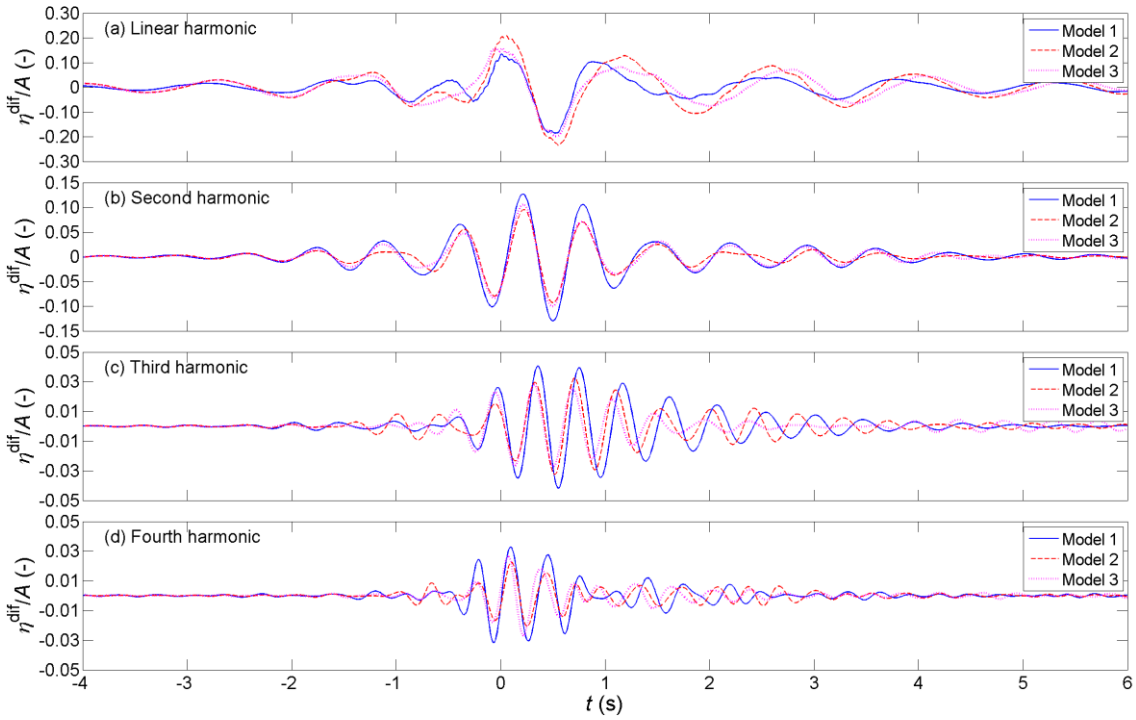

Figure 9. Time histories of the scattered waves near the bow of the models for kA = 0.21 (WG10). Note the different vertical scales.

3.1.2 Near the stern

Wave scattering at the stern of three models is investigated using wave gauges WG4, WG8 and WG22 shown in Figure 6, all of which have the same relative distance from the stern of Models 1, 2 and 3 respectively. The linear and higher-harmonic sum frequency harmonic components are separated by applying the phase-based method as before, and are presented in Figure 10 for the tests with and without models. The amplitude spectra of the linear harmonics with models in place are smaller than those without models (Figure 10a), but the amplitude spectra of the higher harmonics increase with models in place (Figure 10b, c, d). Furthermore, it is shown that the amplitude spectrum of the linear component decreases slightly as model length increases (Figure 10a). The amplitude spectra of the second- and third-harmonic sum frequency terms are highest in the presence of Model 2, while they are approximately the same with Models 1 and 3 (Figure 10b, c). For the fourth-harmonic sum frequency, the amplitude spectra are quite similar in magnitude but rather wiggly for all three models (Figure 10d). The harmonic extraction process is sensitive to the accuracy of the time alignment of the four phase combinations, but the results presented here are very clearly separated between the different harmonics and we cannot see any significant leakage between harmonics.

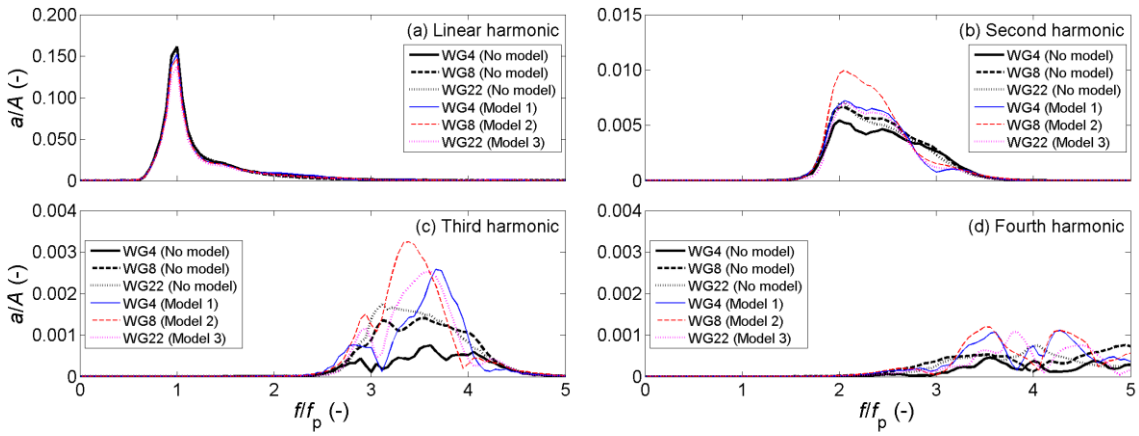

Figure 10. Amplitude spectra of the separated components near the stern for kA = 0.21. Note the different vertical scales.

The time histories of the separated harmonics from the corresponding filtered amplitude spectra are shown in Figure 11. Data are also shown for the test without the models in place for comparison. The linear components are slightly smaller with the models in place (Figure 11a, e, i). The difference in the free surface elevation with and without the models in place is much more significant for the second-, third- and fourth-order sum frequency terms (Figure 11b-d, f-h, j-l). A second wave group due to diffraction from the model is observed in the second-, third- and fourth-harmonic sum frequency terms, and this appears to come later than the first pulse by about 3 s for the second harmonic (Figure 11b, f, j) and about 1.5 s for the third and fourth harmonics (Figure 11c, g, k & Figure 11d, h, l). The second wave packet is significantly lower in amplitude than the first group for the second harmonic (Figure 11b, f, j), while the second pulse is slightly higher than the first pulse for the third-order sum frequency component (Figure 11c, g, k). At the fourth-harmonic sum frequency, the first and second pulses are approximately the same amplitude, and it seems there is a third pulse in the free-surface elevation at about t = 5.5 s (Figure 11d, h, l). The second and third wave packets are clearly separated from and arrive much earlier than the double frequency error wave trains off the wave paddles which arrived at the model position at t = +13 s (Figure 5b).

The time histories of the linear and higher harmonic scattered waves near the stern of the models presented in Figure 12 indicate the effect of wave-structure interaction on the linear component is quite weak (Figure 12a, e, i), but this effect is relatively much stronger for the higher harmonic components (Figure 12b-d, f-h, j-l). The free-surface elevations of second and fourth harmonic scattered waves are reduced as the model length increases (Figure 12b, f, j for the second harmonic & Figure 12d, h, l for the fourth harmonic). For the third harmonic component, the free-surface elevation of the scattered wave is strongest with Model 2 and it is nearly the same with Model 1 and 3 (Figure 12c, g, k).

One may speculate that this is an interference effect with substantial nonlinear scattering off the bow first and later off the stern. Both scattered components reach the downstream offset wave gauges but with different time delays for the different length models, so with different degrees of overlap in time.

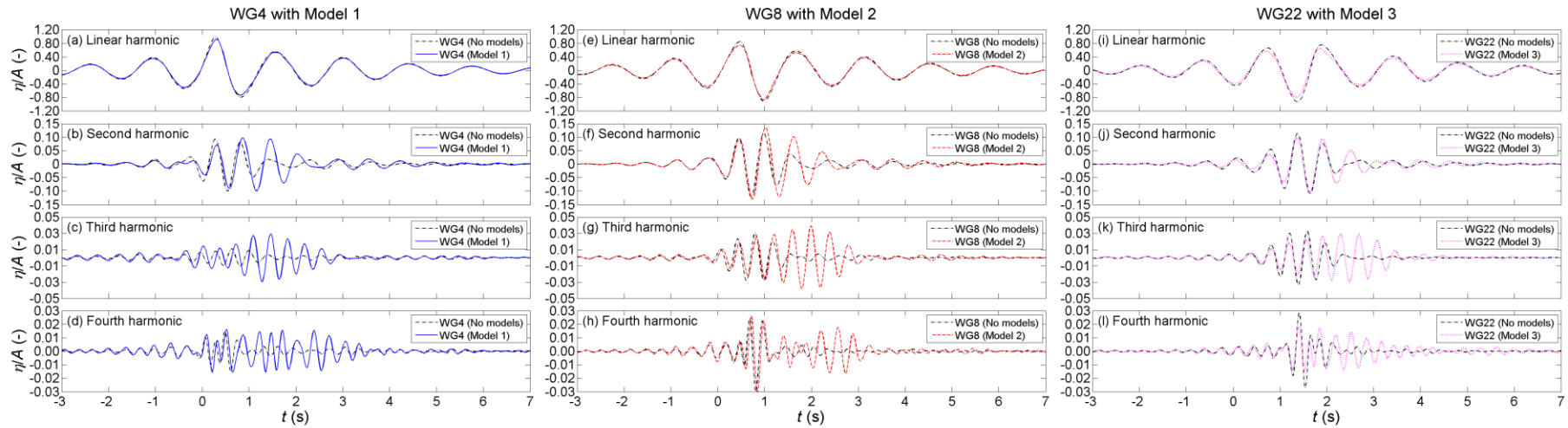

Figure 11. Time histories of the separated components near the stern of the models for kA = 0.21. Note the different vertical scales.

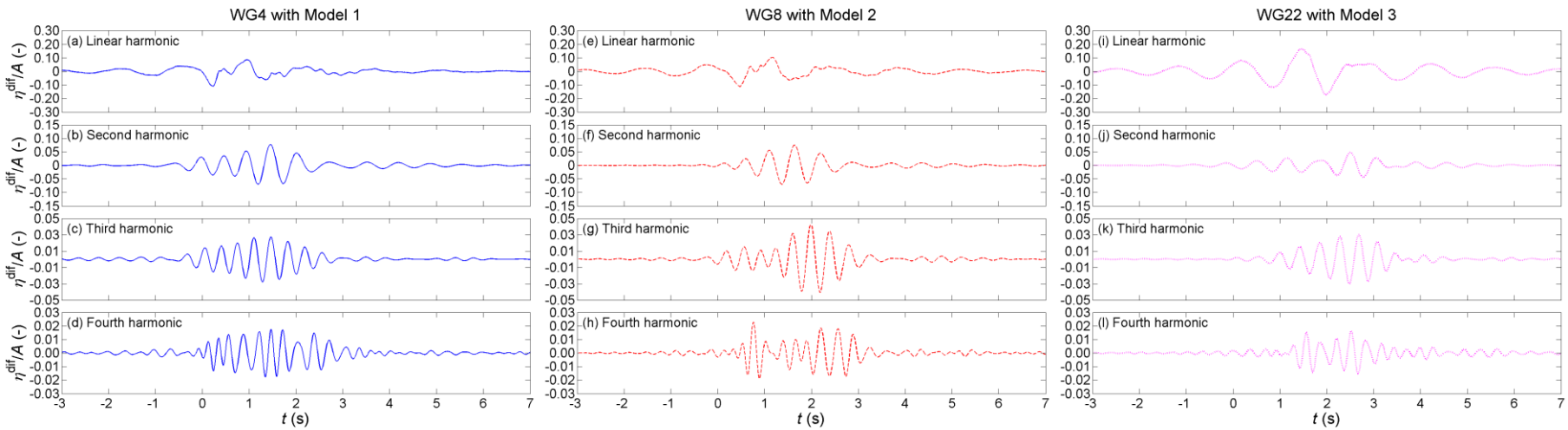

Figure 12. Time histories of the scattered waves near the stern of the models for kA = 0.21. Note the different vertical scales.

3.2 Effect of wave steepness on wave scattering

The input wave groups used in these experiments are defined assuming linear paddle transfer functions and then linear propagation and frequency dispersion on finite depth. For finite amplitude waves, cubic wave-wave interactions can occur which lead to changes in both the amplitude and phase of the waves away from linear predictions. This type of modulational instability was first observed by Benjamin and Feir (1967) for regular waves, see the review by Yuen and Lake (1980). For wave groups these effects are cumulative, increasing at increasing distance from the wave maker (see, for example, Baldock et al., 1996; Ning et al., 2009; and Adcock and Taylor, 2009 & 2016). Since we want to change of the amplitude of the incident packet to explore the amplitude ordering of the various scattered wave harmonics, it is important to establish whether nonlinear evolution is significantly changing the structure of the incident wave group when it interacts with the models.

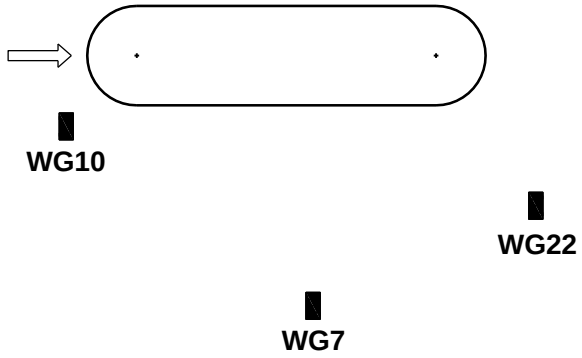

Figure 13. Location of WG7, 10 & 22 w.r.t Model 3.

The effect of wave steepness on the scattering is reported for Model 3, shown in Figure 13, with the focused wave groups of two different steepnesses and three gauge locations: near to the bow (WG10), to the side (WG7) and near to the stern (WG22). Results are presented for wave steepness kA = 0.13 and 0.18.

Time histories of the linear harmonics of the tested focused wave groups with steepness kA = 0.13 and 0.18, at the location near the bow of Model 3 (WG10) but with the model removed are presented in Figure 14. The solid line represents the scaled time history of the linear harmonic of the focused wave group with kA = 0.13 (by a scaling factor of 0.18/0.13 = 1.38), the dashed line for kA = 0.18 and the dotted line is the difference between the solid and dashed lines. It is shown that the solid and dashed lines are almost identical. Therefore, we see no evidence of significant cumulative evolution beyond linear as the wave propagates from the paddle to the position of the model. We can then treat the incident linear components as identical in shape, simply with an amplitude scaling.

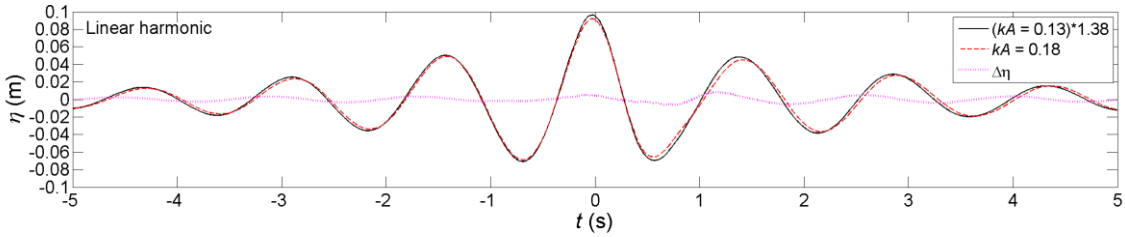

Figure 14. Comparison of the linear component of the tested wave groups (kA = 0.13 & 0.18).

Applying the phase-based separation method presented in Section 2.2, the amplitude spectra of the linear and second, third and fourth harmonics of the separated components are examined. Only the

more interesting higher harmonics are presented in this section to examine the effect of wave steepness on the wave-structure interaction, because the linear component simply scaled with wave steepness, except for a slight difference at the spectral tail high frequencies. Amplitude spectra of the second, third and fourth harmonics of the separated components are presented in Figure 15, Figure 16 and Figure 17 for the location near the bow (WG10), to the side (WG7) and near the stern (WG22) of Model 3, respectively. In general, as would be expected, the amplitude spectra of the higher harmonics are seen to increase as the wave steepness is increased from kA = 0.13 (solid line) to kA = 0.18 (dashed line). The amplitude spectrum of the second harmonic near the bow of the model is significantly higher than those at the side and near the stern (Figure 15a, Figure 16a & Figure 17a), and there is slight difference in the amplitude spectra of the third and fourth harmonic components at those locations (Figure 15b-c, Figure 16b-c & Figure 17b-c). The steepness of the wave appears to have its greatest effect on the third harmonics where some of the values nearly double near the stern (Figure 17b).

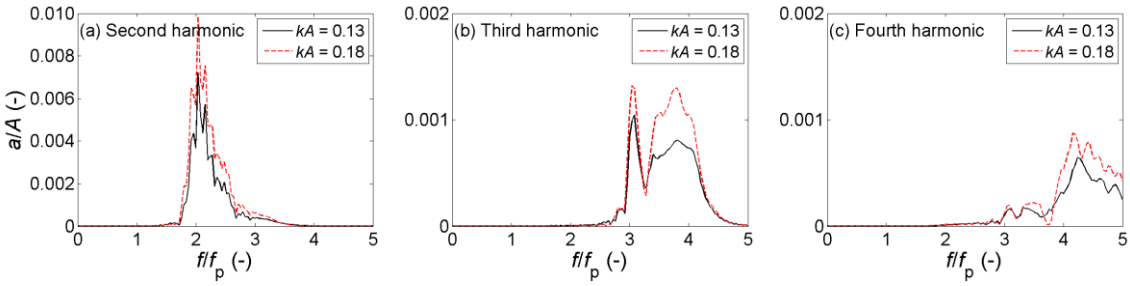

Figure 15. Amplitude spectra of the separated components near the bow of Model 3 (WG10). Note the different vertical scales.

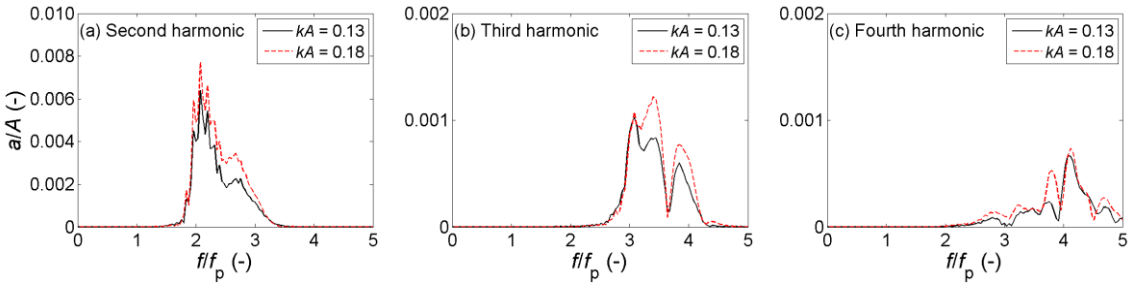

Figure 16. Amplitude spectra of the separated components alongside Model 3 (WG7). Note the different vertical scales.

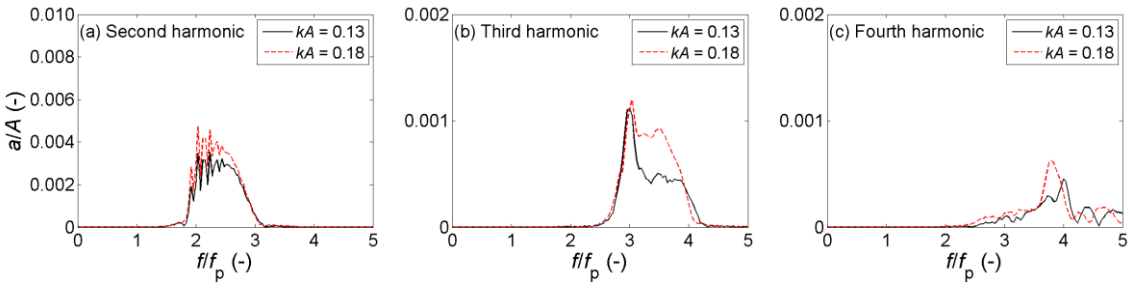

Figure 17. Amplitude spectra of the separated components near the stern of Model 3 (WG22). Note the different vertical scales.

The corresponding filtered time histories of the higher harmonics of the scattered wave fields at locations near the bow, to the side and near the stern of Model 3 are presented in Figure 18, Figure 19 and Figure 20, respectively. At the bow there is considerable amplification of the second and fourth harmonics (Figure 18a, c). A significant effect of the wave steepness can also be found at the third harmonic of the scattered wave near the stern (Figure 20b) as might be expected from the amplitude spectrum. The fourth harmonic component near the bow is much higher than that to the side and near the stern of the model (Figure 18c, Figure 19c and Figure 20c). This is at least due to

WG10 being closer to the model so the radiated field has not decayed in amplitude significantly due to geometric spreading, whereas for the other gauge positions spreading is more important.

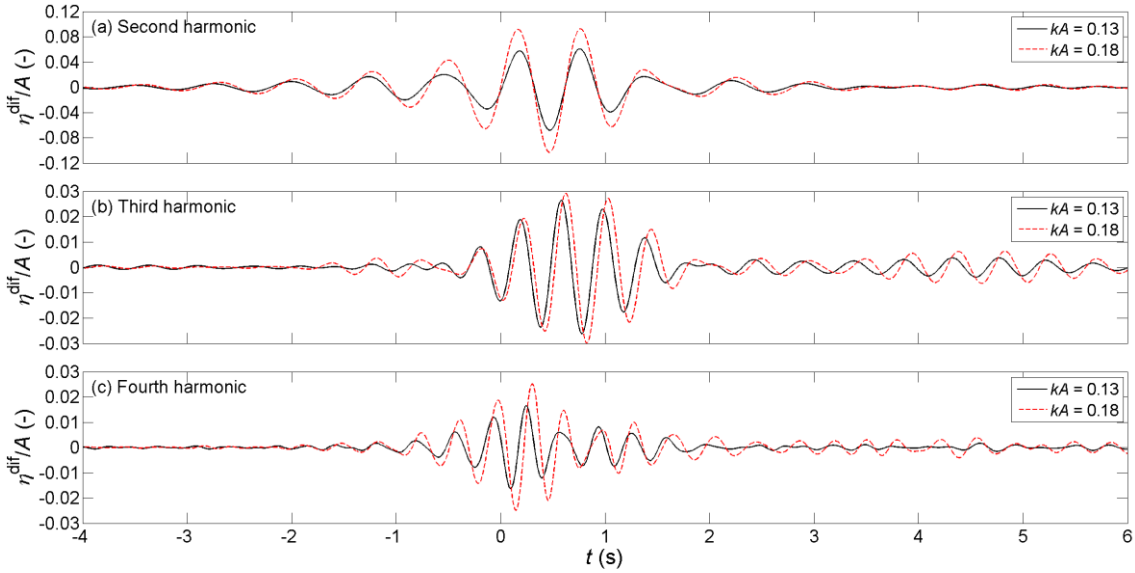

Figure 18. Time histories of the scattered waves near the bow of Model 3 (WG10). Note the different vertical scales.

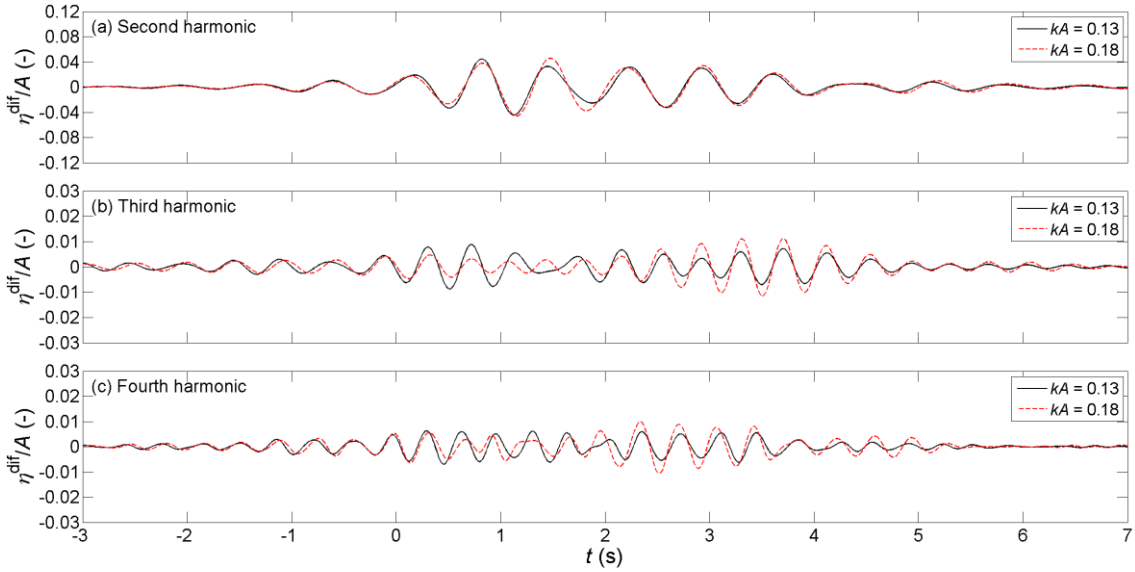

Figure 19. Time histories of the scattered waves alongside Model 3 (WG7). Note the different vertical scales.

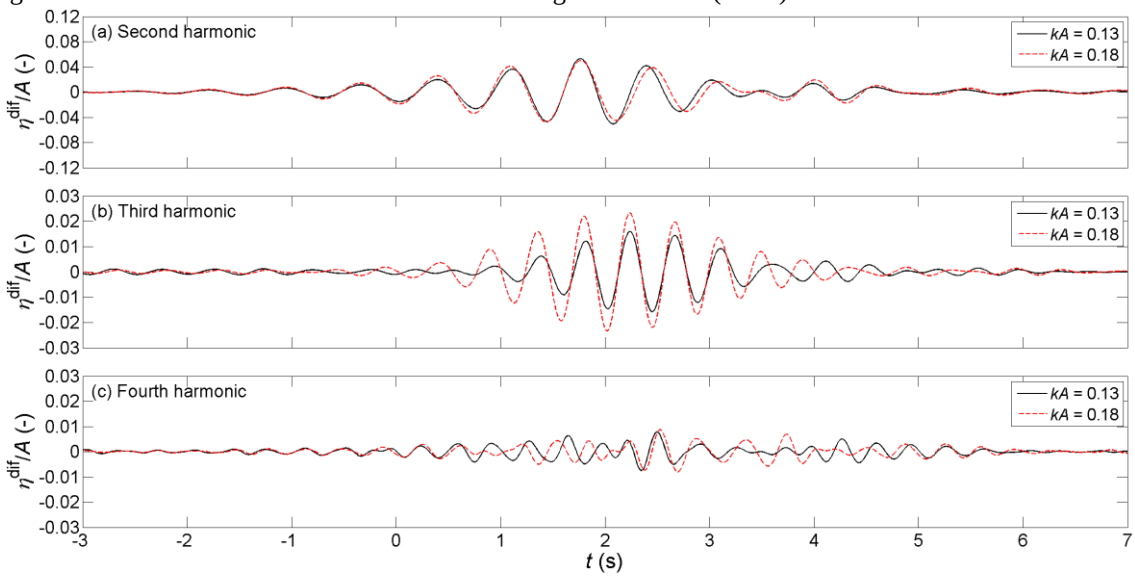

Figure 20. Time histories of the scattered waves near the stern of Model 3 (WG22). Note the different vertical scales.

3.3 Effect of incident wave angle on wave scattering

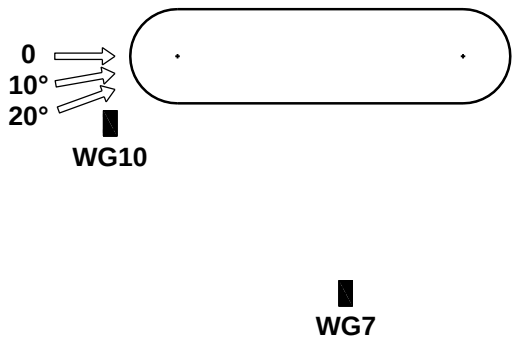

Figure 21. The tested incident wave angles with model 3.

Different incident wave angles were tested to investigate the effect of wave direction on scattering. Tests were conducted with incident wave directions of 0°, 10° and 20° (Figure 21) with a wave steepness kA = 0.17. In this case, only the crest focused wave group (η^0) and the trough focused wave group (η^{180}) were tested. Therefore, the odd and even harmonics were separated using the simple phase-inversion separation method which has been presented in previous studies (Baldock et al., 1996; Zang et al., 2006; Fitzgerald et al., 2014).

$$(\eta^0 - \eta^{180})/2 = \eta_{11} + \eta_{31} + \eta_{33} \quad (8)$$

$$(\eta^0 + \eta^{180})/2 = \eta_{20} + \eta_{40} + \eta_{22} + \eta_{42} + \eta_{44} \quad (9)$$

The odd and even harmonics are separated using Equation (8) and (9), respectively. Frequency filtering is applied to extract the higher harmonic amplitude spectra from the odd and even harmonics, and then the free-surface elevations of those higher harmonic terms ($\eta_{22}+\eta_{42}$, η_{33}, η_{44}) are obtained using inverse FFT of the filtered amplitude spectra.

Amplitude spectra of the linear and the higher harmonic components for the location near the bow (WG10) and to the side (WG7) of Model 3, due to different incident wave angles, are presented in Figure 22 and Figure 23, respectively. It can be seen that the amplitude spectra of the harmonic components increase as the incident wave angle increases from 0° to 20°, but are most energetic at the incident angle of 10°, except for the third harmonic to the side where the amplitude spectrum decreases with increasing the wave angle (Figure 23c).

It is striking that the amplitude spectra are generally of comparable shape for the linear and second harmonics, as the approaching direction is altered. In contrast, the shape of the fourth harmonic spectrum changes somewhat and the third harmonic spectrum changes significantly, suggesting that third harmonic is in some sense ‘different’.

The time histories of the scattered wave corresponding to the amplitude spectra near the bow and to the side are presented in Figure 24 and Figure 25. The linear, third and fourth harmonics are reduced with increasing angle of incidence for both locations (Figure 24a, c, d and Figure 25a, c, d). On the contrary, the second harmonic is greatest for the 10° wave (Figure 24b and Figure 25b). The third and fourth harmonics at the location near the bow (Figure 24c, d) are significantly larger than those to the side of the model (Figure 25c, d).

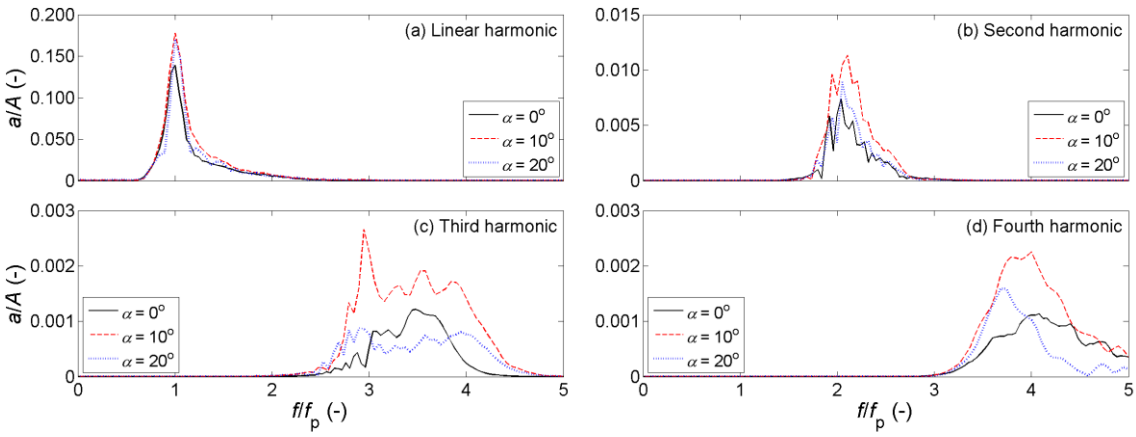

Figure 22. Amplitude spectra of the separated components near the bow of Model 3 for *kA* = 0.17 (WG10). Note the different vertical scales.

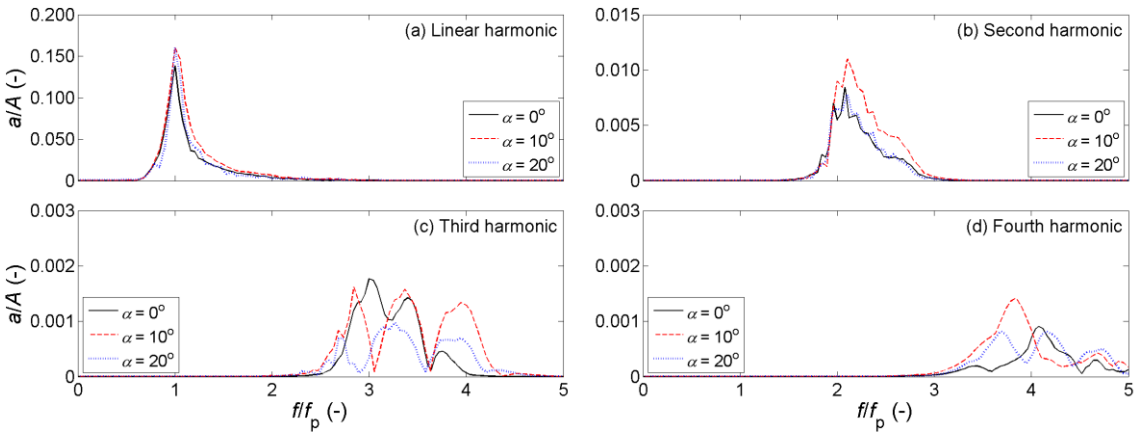

Figure 23. Amplitude spectra of the separated components alongside of Model 3 for *kA* = 0.17 (WG7). Note the different vertical scales.

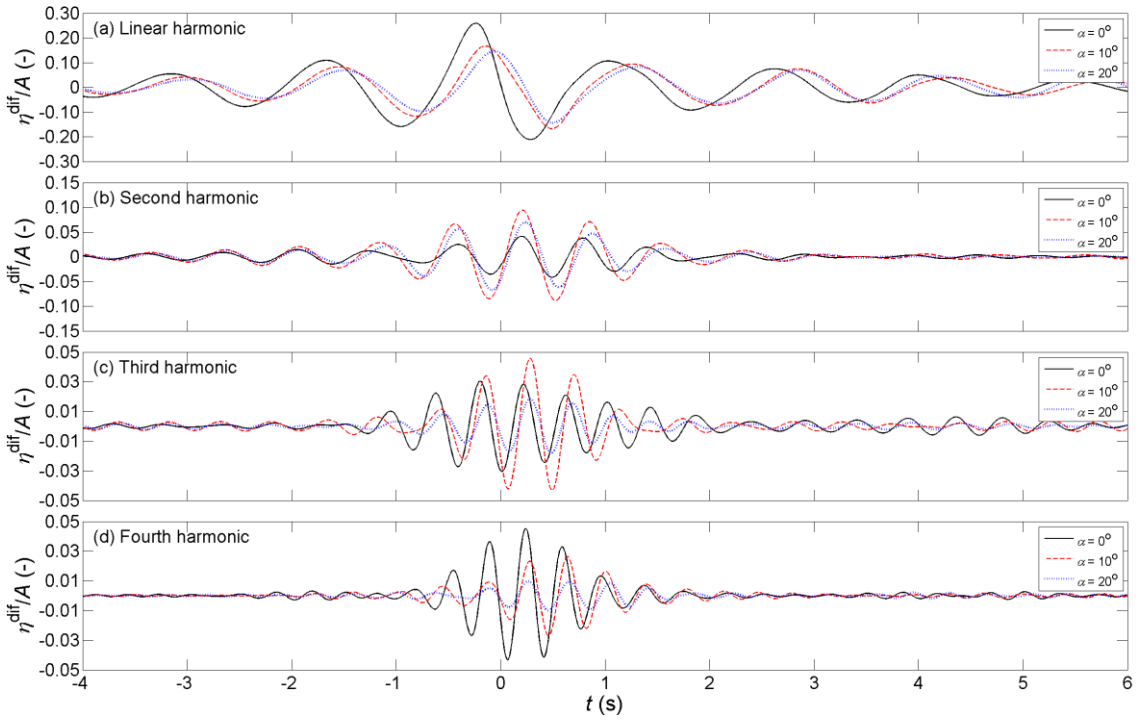

Figure 24. Time histories of the scattered waves near the bow of Model 3 for *kA* = 0.17 (WG10). Note the different vertical scales.

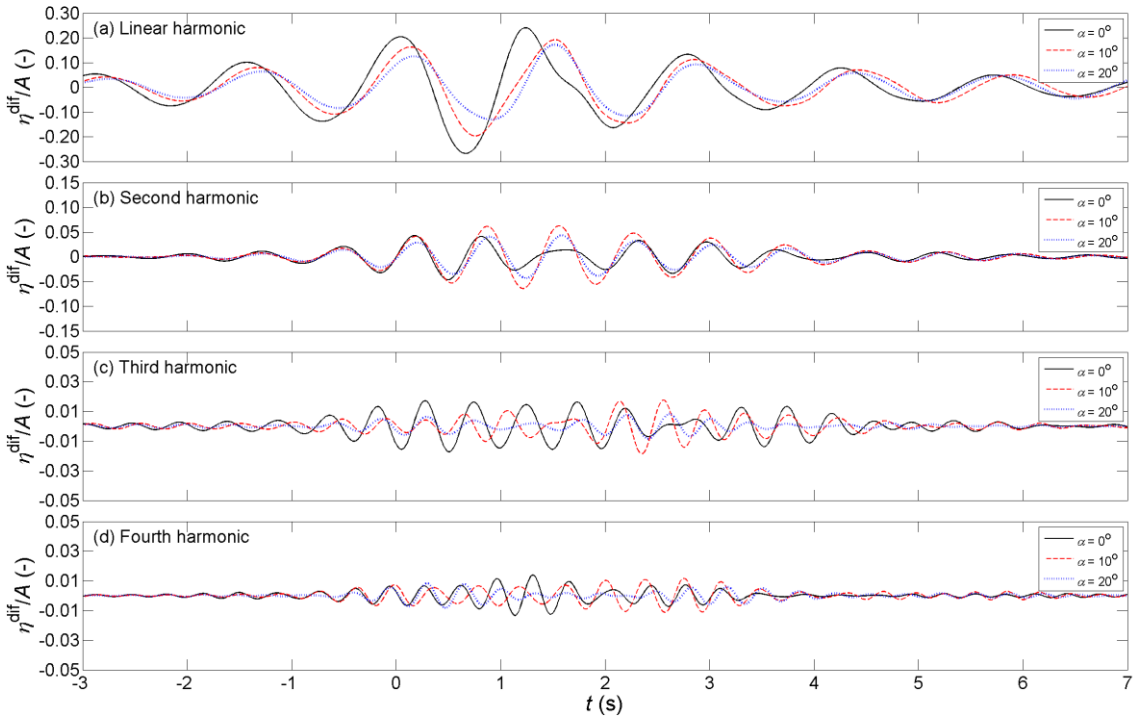

Figure 25. Time histories of the scattered waves alongside of Model 3 for kA = 0.17 (WG7). Note the different vertical scales.

4 Discussion of the results

This experimental work has shown that there are the second, third and fourth harmonic scattered waves upstream of the bow, out to the side and downstream of all three tested models. These findings are consistent with Fitzgerald et al. (2014) where their analysis of a 0.25 m diameter cylinder interacting with a focused wave group with kA = 0.1 gives results with strong similarities to Model 1 (Figures 8, 9, 11 and 12). However, their analysis of the cylinder simulations did not stress the structure of the fourth harmonic components, due to concerns about grid resolution. Similar second harmonic scattered waves were also found on the upstream side of a FPSO model, which is similar to Model 3 in this paper, by Zang et al. (2006) and Siddorn (2012), but their work did not identify significant third and fourth harmonic scattered waves on the upstream side comparable to our experimental observations for Model 3 (Figure 8, 9 and 18). Siddorn (2012) simulated wave-structure interaction of the FPSO model presented by Zang et al. (2006) and found a third harmonic scattered wave to the side and downstream of the FPSO model comparable to those reported here (Figure 11, 12, 19 and 20). In the present study, a second wave packet in the second, third and fourth harmonics has been found at almost all the observed locations surrounding the models. These second pulses are entirely separate from and occur much earlier than the error wave train off the wave paddles. So these second pulses are excited by the main incident group, and they may induce a second load cycle on the structure.

The linear, second, third and fourth harmonic scattered waves near the bow of models in our experiment increased their maximum amplitudes by 21%, 13%, 4% and 3% of the undisturbed incident linear amplitude, respectively (Figure 9). These components are much larger at locations closer to the bow of the model i.e. at WG16 located at 0.01 m from the bow (see Figure 2). At this location, effectively the front stagnation point, the linear, second, third and fourth harmonic scattered wave amplitudes increase up to 33%, 27%, 8% and 4% of the incident linear wave, respectively (Figure 26). Zang et al. (2006) found that near the bow the linear and second order diffraction increased by 45% and 30% the undisturbed incident crest elevation and these are quite

similar to our findings here. The linear and higher harmonic scattered wave amplitudes near the stern of the models are comparable with those near the bow, except for the linear components at the stern (WG24 in Figure 2) of Model 1 and 2. These increase by up to 120% and 90% the undisturbed incident linear wave amplitude (Figure 27) and it is clearly seen that the model length significantly affects the linear diffraction term at the stern (the shorter the model length the higher the linear diffraction). The fourth harmonic scattered wave amplitude can be seen to be as much as 8% of the undisturbed incident linear component if the two phase separation method is applied (Figure 24). Evidence of the second scattered wave packets is also found for the third and fourth harmonics at the bow, from t = +1 s to +4 s (Figure 26c, d), and at the stern, from t = +2.5 s to +5.5 s (Figure 27c, d), of the models. It would be expected that the higher harmonic wave field saturates when the input wave amplitude is sufficiently large (Grue, 1992), but these present tests are likely to be well short of this stage when the whole idea of a Stokes-type expansion breaks down.

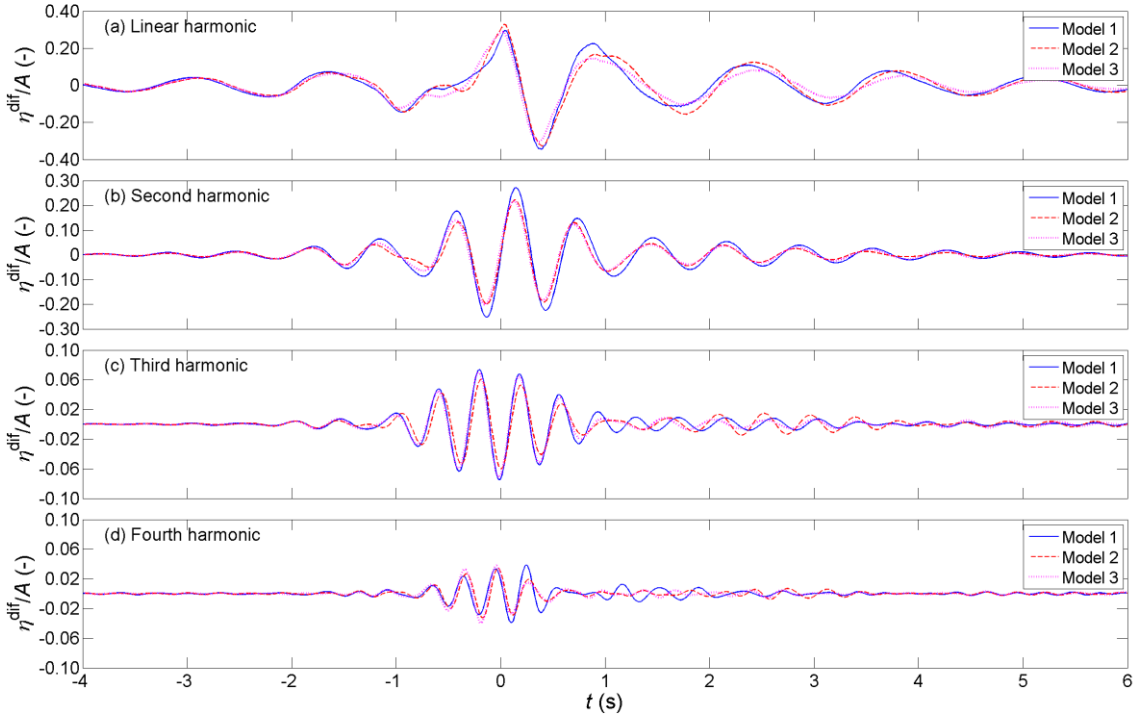

Figure 26. Time histories of the scattered waves at the bow of the models for kA = 0.21 (WG16). Note the different vertical scales.

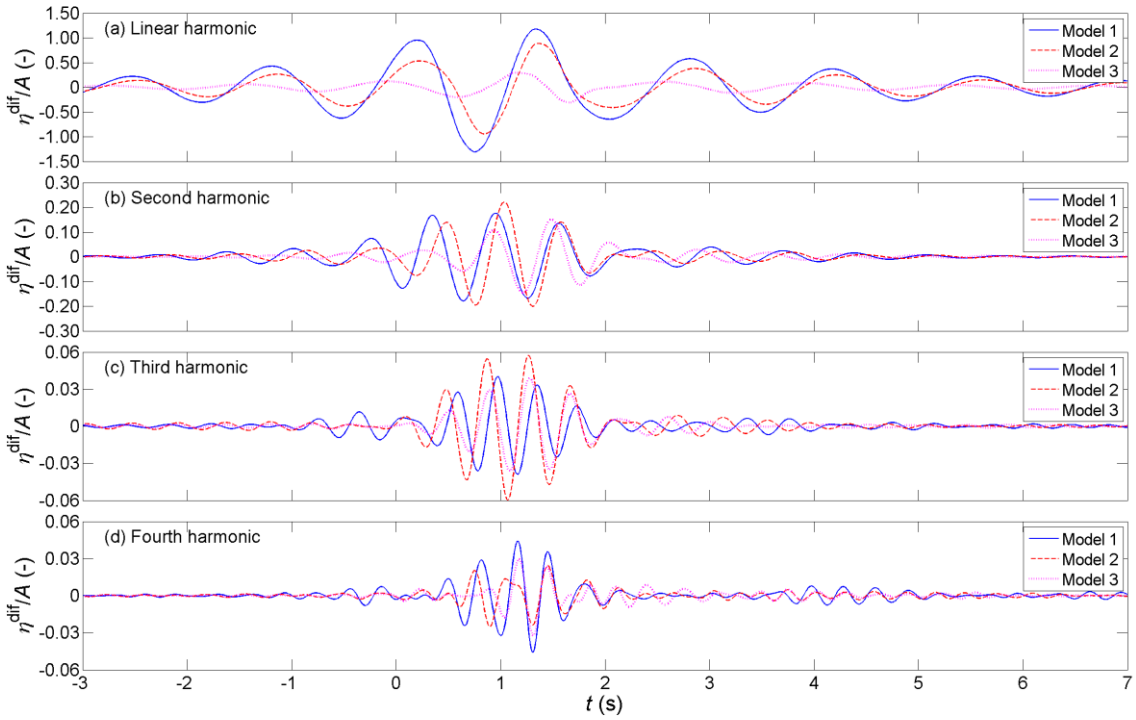

Figure 27. Time histories of the scattered waves at the stern of the models for kA = 0.21 (WG24). Note the different vertical scales.

The interaction of the incoming wave group with the bow of each of the models results in a second difference frequency component (η_{20}). This is a long bound wave and significantly contributes to the local free surface elevation at the bow (up to about 10% of the undisturbed linear harmonic amplitude), see Figure 28, 29 and 30. It is interesting to see that there is a considerable set-*up* of the water surface at the bow (focal location) with each of the models in place, and this should be contrasted with the smaller set-*down* at the focal location without the models (Figure 28). This behaviour of the second difference component with and without models is similar to the results presented in Zang et al. (2006) where they showed the excellent agreement between the experiments and second-order diffraction calculations. Figure 28 also shows that the local second difference component set-*up* is unaffected by the model lengths. Indeed, with three different lengths of the models (Models 1, 2 and 3), the second difference components are almost identical at the bow. In contrast, the second difference component is dependent on the wave steepness and wave direction, scaling simply as the square of the wave group linear amplitude (again consistent with 2nd order diffraction) as shown in Figure 29. Furthermore, it is unchanged with wave direction from head-on α = 0° to an approach angle of 10°, but reduced at least at the gauge position for a wave approach angle of α = 20° off head-on, as shown in Figure 30.

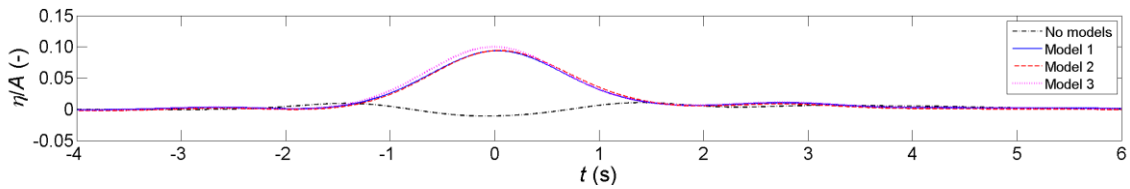

Figure 28. Time histories of the second difference component (η_{20}) at the bow of the models (WG16) for kA = 0.21.

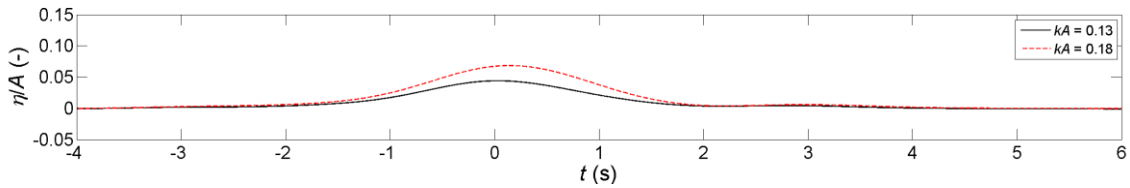

Figure 29. Time histories of the second difference component (η_{20}) at the bow of Model 3 (WG16) for kA = 0.13 & 0.18.

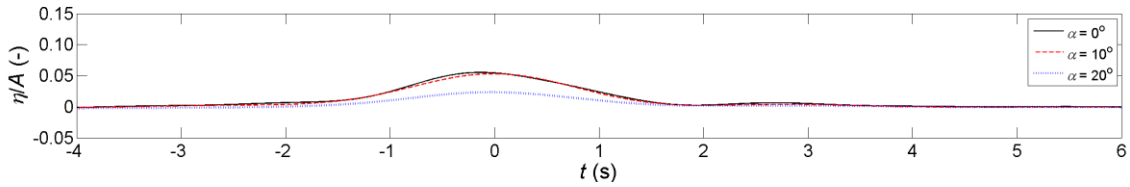

Figure 30. Time histories of the second difference component (η_{20}) at the bow of Model 3 (WG16) for kA = 0.17 and α = 0°, 10° & 20°.

In practical applications, the third- and fourth-order frequency components obtained from the model test should be taken into account to assess wave loading for offshore structure design and the assessment of load components that might produce ringing-type structural responses in fixed and taut moored structures, and numerical modelling should be carefully designed to make sure these effects can be captured. Some traditional numerical modelling approaches are based on linear theory and cannot predict these strongly nonlinear effects (Det Norske Veritas, 2010) and so high order or fully nonlinear approaches should be taken. The effects on crest elevation, which is contributed from the linear, superharmonics (up to fourth-order) and the second difference component (η_{20}), should also be considered for design of the air gap and position of accommodation in offshore structures.

5 Conclusions

Experiments have been performed to examine wave-structure interactions for simplified FPSO geometries. These explore the effects of model length, wave steepness and the incident wave angle on the structure of the total local wave field and also the scattered wave components. An existing general phase-based harmonic separation method has been successfully applied to extract the linear and higher harmonic wave components of the free-surface elevation around the models. The key findings of this study are as follows.

- At locations having the same relative distance to the bow of the models, the highest amplitude scattered waves are obtained with the shortest model (the cylinder). In each case, the second harmonic scattered wave field is comparable in magnitude to the component in undisturbed incident wave, whereas the third- and fourth harmonics are significantly larger than the equivalent incident bound components.
- At locations having the same relative distance to the stern, the linear harmonic increases as model length decreases but the nonlinear harmonics are similar for all three models and slightly smaller for the longest model at the second harmonic component.
- As the incident wave steepness increased, the non-linear scattered wave increases and a second pulse is evident in the higher harmonics of the scattered wave fields (at second-, third- and fourth-order).

- It is found that the second harmonic scattered wave is greatest near the bow for the incident wave angle of 10° and the third and fourth harmonic scattered waves reduce as the incident wave angle increases from 0° to 20°. The incident wave angle affects the maximum crest height and wave loading and therefore it should be considered in design.
- The second order difference long-wave component is a robust feature of our experiments. This interaction produces a substantial and relatively long-lasting set-up at the bow for all three models. All other higher frequency components ride on the local hill, so the implications of this behaviour for green water on deck are clear.
- In a generic sense, we observe that the third harmonic of the scattered wave field shows the most complex structure in time, and also in the spectrum. This is consistent with the discussion of the extra complexity of the third harmonic force component in time on a single cylinder given by Fitzgerald et al. (2014).
- We hope that these experimental results will prove to be of use to modellers of wave-structure interactions for FPSO-type floating bodies; the data will be archived online as required by the Engineering and Physical Science Research Council (EPSRC) and is available by contacting the authors at the University of Plymouth.
- Although these results are for contributions to the surface elevation around the models, the third- and fourth-order wave components contribution to global force and to local pressures on the body surface should also be considered for assessing wave loading and structural responses in offshore structure design, which may include ringing-type response effects for some structures.
- Higher order components i.e. the third and four harmonics are significant (up to 8% of overall crest height) so a design method that includes these effects should be applied. This could be achieved using a fully nonlinear numerical method (CFD) solving the Navier-Stokes equations, high-order BEM or FEM schemes for fully nonlinear potential flow, and of course more physical experiments.
- The contributions of the third- and fourth-harmonics and the second difference term to the surface elevation need to be taken into account in design of the air gap and the level of accommodation for offshore structures.

Acknowledgements

This study is a part of the FROTH (Fundamentals and Reliability of Offshore sTructure Hydrodynamics) project supported by the Engineering and Physical Science Research Council (EPSRC Grant EP/J012866/1). The FROTH project is being led by Plymouth University and the collaborative partners include Oxford University, University of Bath, City University London and the Manchester Metropolitan University. The authors gratefully acknowledge the financial support provided by EPSRC and useful discussions with the project partners.

References

Adcock, T.A.A., Taylor, P.H. (2009). "Focusing of unidirectional wave groups on deep water: An approximate nonlinear Schrödinger equation-based model." *Proceedings of the Royal Society A: Mathematical, Physical and Engineering Sciences*, 465 (2110), pp. 3083-3102. (2009)

Adcock, T.A.A. and Taylor, P.H. and Gibbs, R. (2016) “Non-linear evolution of uni-directional focussed wave-groups on deep water: A comparison of models.” *Applied Ocean Research* 59, 147-152.

Bachynski, E. E. and Moan, T. (2014). "Ringing loads on tension leg platform wind turbines." *Ocean Engineering* **84**: 237-248.

Baldock, T. E., Swan, C., Taylor, P. H. (1996). "A Laboratory Study of Nonlinear Surface Waves on Water." Philosophical Transactions of the Royal Society of London A: Mathematical, Physical and Engineering Sciences **354**(1707): 649-676.

Benjamin, T. Brooke; Feir, J.E. (1967). “The disintegration of wave trains on deep water. Part 1. Theory.” *Journal of Fluid Mechanics* **27** (3): 417-430.

Borthwick, A. G. L., Hunt, A. C., Feng, T., Taylor, P. H., Stansby, P. K. (2006). "Flow kinematics of focused wave groups on a plane beach in the U.K. Coastal Research Facility." Coastal Engineering **53**(12): 1033-1044.

Det Norske Veritas (2010). “Environmental conditions and environmental loads”. Recommended Practice DNV-RP-C205.

Faltinsen, O. M., Newman, J. N. and Vinje, T. (1995). “Nonlinear wave loads on a slender vertical cylinder.” *Journal of Fluid Mechanics*, **289**, pp 179-198.

Faltinsen, O. M. (2014). "Hydrodynamics of marine and offshore structures." *Journal of Hydrodynamics*, Ser. B **26**(6): 835-847.

Fenton, J. D. (1985). “A fifth-order Stokes theory for steady waves.” *J. Waterway Port Coastal and Ocean Engineering. ASCE*. **111**: 216-234.

Fitzgerald, C. J., Taylor, P. H., Taylor, R. E., Grice, J., Zang, J. (2014). "Phase manipulation and the harmonic components of ringing forces on a surface-piercing column." *Proceedings of the Royal Society of London A: Mathematical, Physical and Engineering Sciences* **470**(2168)

Grue, J. (1992). “Nonlinear water waves at a submerged obstacle or bottom topography.” *Journal of Fluid Mechanics*, **244**, pp 455-476.

Hann, M., Greaves, D., Raby, A. (2014). “A new set of focused wave linear combinations to extract non-linear wave harmonics.” *In Twenty-ninth Int. Workshop on Water Waves and Floating Bodies*, Osaka, Japan, 30 March - 2 April, 61–64 (http://www.iwwwfb.org/Abstracts/iwwwfb29/iwwwfb29_16new.pdf)

HR Wallingford Ltd (2002). “FPSO response in long and short crested seas.” *HSE OT Report 2002/018*.

Huseby M., Grue J. (2000). “An experimental investigation of higher-harmonic wave forces on a vertical cylinder”. *Journal of Fluid Mechanics*, **414**: 75-103.

Hunt, A., P. H. Taylor, Borthwick, A., Stansby, P., Feng, T. (2003). “Kinematics of a Focused Wave Group on a Plane Beach: Physical Modelling in the UK Coastal Research Facility.” *Coastal Structures* **2003**: 740-750.

Mercier, J. A. (1982). “Evolution of tension leg platform technology.” *Proc 3rd Int. Conf. Behaviour of Offshore Structures*, Massachusetts Institute of Technology, Cambridge, MA.

Ning, D.Z., Zang, J., Liu, S.X., Eatock Taylor, R., Teng, B., Taylor, P.H. (2009). “Free-surface evolution and wave kinematics for nonlinear uni-directional focused wave groups.” *Ocean Engineering*, 36 (15-16), pp. 1226-1243.

Offshore Technology Report (2001). "Environmental considerations." *Health and Safety Executive*, OT 2001/010, pp 82.

Siddorn, P. D. (2012). “Efficient numerical modelling of wave-structure interaction.” DPhil. University of Oxford.

Shao Y. L., Faltinsen O. M. (2014). “A harmonic polynomial cell (HPC) method for 3D Laplace equation with application in marine hydrodynamics.” *Journal of Computational Physics*, **274**: 312-332.

Tromans, P.S., Anaturk, A.R., and Hagemeijer, P. (1991). “A new model for the kinematics of large ocean waves - application as a design wave.” *Proc. 1st Int. Offshore and Polar Eng. Conf.*, Edinburgh, U.K., 11-16 August, 64-71.

Williams, M. O. (2008). “Wave mapping in UK waters: Supporting document.” *Health and Safety Executive*, Research Report RR621, pp 38.

Yuen, H.C.; Lake, B.M. (1980). “Instabilities of waves on deep water.” *Annual Review of Fluid Mechanics* **12**: 303-334.

Zang, J., Gibson, R., Taylor, P. H., Eatock Taylor, R., and Swan, C. (2006). “Second order wave diffraction around a fixed ship-shaped body in unidirectional steep waves.” *Journal of Offshore Mechanics and Arctic Engineering*, **128**(2): 89.